Evidence for sub-Chandrasekhar-mass progenitors of Type Ia supernovae at the faint end of the width–luminosity relation

Stéphane Blondin, Luc Dessart, D. John Hillier, Alexei M. Khokhlov

MNRAS 000, 1–8 (2017) Preprint 13 November 2018 Compiled using MNRAS LATEX style file v3.0

Evidence for sub-Chandrasekhar-mass progenitors of Type Ia supernovae at the faint end of the width-luminosity relation

Stéphane Blondin,[1]★ Luc Dessart,[2] D. John Hillier,[3] and Alexei M. Khokhlov[4]
[1]Aix Marseille Univ, CNRS, LAM, Laboratoire d'Astrophysique de Marseille, Marseille, France
[2]Unidad Mixta Internacional Franco-Chilena de Astronomía (CNRS UMI 3386), Departamento de Astronomía, Universidad de Chile, Camino El Observatorio 1515, Las Condes, Santiago, Chile
[3]Department of Physics and Astronomy & Pittsburgh Particle Physics, Astrophysics, and Cosmology Center (PITT PACC), University of Pittsburgh, Pittsburgh, PA 15260, USA
[4]Department of Astronomy & Astrophysics, the Enrico Fermi Institute, and the Computation Institute, The University of Chicago, Chicago, IL 60637, USA

Accepted 2016 September 28. Received 2016 September 02; in original form 2016 June 24

ABSTRACT

The faster light-curve evolution of low-luminosity Type Ia supernovae (SNe Ia) suggests that they could result from the explosion of white dwarf (WD) progenitors below the Chandrasekhar mass ($M_{\rm Ch}$). Here we present 1D non-local thermodynamic equilibrium time-dependent radiative transfer simulations of pure central detonations of carbon-oxygen WDs with a mass ($M_{\rm tot}$) between 0.88 $M_\odot$ and 1.15 $M_\odot$, and a ^{56}Ni yield between 0.08 $M_\odot$ and 0.84 $M_\odot$. Their lower ejecta density compared to $M_{\rm Ch}$ models results in a more rapid increase of the luminosity at early times and an enhanced γ-ray escape fraction past maximum light. Consequently, their bolometric light curves display shorter rise times and larger post-maximum decline rates. Moreover, the higher $M(^{56}{\rm Ni})/M_{\rm tot}$ ratio at a given ^{56}Ni mass enhances the temperature and ionization level in the spectrum-formation region for the less luminous models, giving rise to bluer colours at maximum light and a faster post-maximum evolution of the $B-V$ colour. For sub-$M_{\rm Ch}$ models fainter than $M_B \approx -18.5$ mag at peak, the greater bolometric decline and faster colour evolution lead to a larger B-band post-maximum decline rate, $\Delta M_{15}(B)$. In particular, all of our previously-published $M_{\rm Ch}$ models (standard and pulsational delayed detonations) are confined to $\Delta M_{15}(B) < 1.4$ mag, while the sub-$M_{\rm Ch}$ models with $M_{\rm tot} \lesssim 1\,M_\odot$ extend beyond this limit to $\Delta M_{15}(B) \approx 1.65$ mag for a peak $M_B \approx -17$ mag, in better agreement with the observed width-luminosity relation (WLR). Regardless of the precise ignition mechanism, these simulations suggest that fast-declining SNe Ia at the faint end of the WLR could result from the explosion of WDs whose mass is significantly below the Chandrasekhar limit.

Key words: radiative transfer – supernovae: general

1 INTRODUCTION

The finding that the peak magnitudes of Type Ia supernovae (SNe Ia) are tightly correlated with their post-maximum decline rate in several optical bands (Pskovskii 1977; Phillips 1993) revolutionized the use of these events as extra-galactic distance indicators and formed the cornerstone for the discovery of dark energy (Riess et al. 1998; Perlmutter et al. 1999).

Due to its determining role in observational cosmology, this so-called width-luminosity relation (hereafter WLR when considering the B-band) has received extensive theoretical attention. The slower post-maximum decline of SNe Ia with larger peak M_B has been thought to arise from an increase in opacity with ^{56}Ni mass, which affects the timescale for the radiation to escape the ejecta (e.g., Hoeflich et al. 1996; Pinto & Eastman 2001; Mazzali et al. 2001). However, in contrast with observational studies that show a significantly weaker relation between peak magnitude and post-maximum decline rate for the integrated $(U)BVRI$ flux (e.g., Contardo et al. 2000), one would expect this relation to also hold for the bolometric luminosity.

A later study by Kasen & Woosley (2007) showed that the decay heating from ^{56}Ni affects the onset of the III→II recombination of iron-group elements (IGEs) in the ejecta, which causes a faster colour evolution for the least luminous events (in particular the $B-V$ colour), and hence a larger decline rate in B relative to other bands. The WLR is then interpreted purely as a colour effect related to the level of Fe II/Co II line blanketing, independent of the evolution of the bolometric luminosity.

The mass of the exploding WD (hereafter $M_{\rm tot}$) is known to affect the bolometric evolution around maximum light

★ E-mail: stephane.blondin@lam.fr

Table 1. Basic properties of the SN Ia models considered in this study, with photometric quantities relevant to the width-luminosity relation.

Model	$M_{\rm tot}$ ($M_\odot$)	$E_{\rm kin}$ (erg)	$M(^{56}{\rm Ni})$ ($M_\odot$)	$v_{99}(^{56}{\rm Ni})$ (km s^{-1})	$\dot{e}_{\rm decay}$ (erg s^{-1} g^{-1})	$t_{\rm rise}$(bol) (day)	$t_{\rm rise}(B)$ (day)	$L_{\rm bol}$ (erg s^{-1})	M_B (mag)	ΔM_{15}(bol) (mag)	$\Delta M_{15}(B)$ (mag)	$(B-V)_{+0}$ (mag)	$(B-V)_{+15}$ (mag)
Standard Chandrasekhar-mass delayed-detonation models (DDC series)													
DDC0	1.41	1.56 (51)	0.86	1.29 (4)	6.32 (9)	16.7	17.7	1.85 (43)	−19.65	0.74	0.74	0.02	0.20
DDC6	1.41	1.50 (51)	0.72	1.20 (4)	5.41 (9)	16.8	18.0	1.57 (43)	−19.48	0.72	0.83	0.04	0.36
DDC10	1.41	1.48 (51)	0.62	1.15 (4)	4.63 (9)	17.1	17.7	1.38 (43)	−19.33	0.74	0.92	0.04	0.50
DDC15	1.41	1.47 (51)	0.51	1.12 (4)	3.72 (9)	17.6	17.1	1.14 (43)	−19.15	0.72	1.03	0.04	0.65
DDC17	1.41	1.41 (51)	0.41	1.08 (4)	2.85 (9)	18.6	17.2	9.10 (42)	−18.93	0.67	1.27	0.04	0.90
DDC20	1.41	1.38 (51)	0.30	1.03 (4)	2.12 (9)	18.7	17.2	6.65 (42)	−18.44	0.58	1.38	0.28	1.14
DDC22	1.41	1.30 (51)	0.21	9.80 (3)	1.40 (9)	19.6	17.5	4.47 (42)	−17.62	0.54	1.22	0.73	1.34
DDC25	1.41	1.18 (51)	0.12	8.56 (3)	7.37 (8)	21.0	19.8	2.62 (42)	−16.44	0.62	1.01	1.31	1.50
Pulsating Chandrasekhar-mass delayed-detonation models (PDDEL series)													
PDDEL1	1.38	1.35 (51)	0.75	1.33 (4)	5.87 (9)	16.4	18.0	1.62 (43)	−19.49	0.76	0.95	0.07	0.51
PDDEL3	1.38	1.33 (51)	0.68	1.30 (4)	5.30 (9)	16.6	18.1	1.48 (43)	−19.39	0.76	1.04	0.08	0.62
PDDEL7	1.38	1.32 (51)	0.60	1.29 (4)	4.72 (9)	16.6	17.8	1.32 (43)	−19.25	0.72	1.12	0.10	0.77
PDDEL4	1.38	1.30 (51)	0.53	1.27 (4)	4.10 (9)	16.9	17.6	1.16 (43)	−19.09	0.69	1.22	0.14	0.90
PDDEL9	1.38	1.26 (51)	0.40	1.23 (4)	3.07 (9)	17.5	16.9	8.81 (42)	−18.70	0.63	1.28	0.27	1.10
PDDEL11	1.38	1.23 (51)	0.30	1.18 (4)	2.13 (9)	18.8	16.9	6.42 (42)	−18.12	0.60	1.21	0.56	1.27
PDDEL12	1.38	1.21 (51)	0.25	1.15 (4)	1.73 (9)	19.5	17.3	5.43 (42)	−17.76	0.60	1.14	0.76	1.35
Sub-Chandrasekhar-mass models (SCH series)													
SCH7p0	1.15	1.40 (51)	0.84	1.51 (4)	7.91 (9)	15.6	15.8	1.85 (43)	−19.64	0.85	0.79	0.06	0.12
SCH6p5	1.13	1.35 (51)	0.77	1.44 (4)	7.43 (9)	15.8	16.2	1.71 (43)	−19.58	0.86	0.81	0.05	0.14
SCH6p0	1.10	1.30 (51)	0.70	1.39 (4)	6.91 (9)	16.0	16.7	1.57 (43)	−19.50	0.86	0.83	0.05	0.17
SCH5p5	1.08	1.23 (51)	0.63	1.32 (4)	6.31 (9)	16.3	17.3	1.42 (43)	−19.39	0.87	0.90	0.06	0.26
SCH5p0	1.05	1.16 (51)	0.55	1.25 (4)	5.67 (9)	16.4	17.3	1.25 (43)	−19.25	0.87	0.97	0.06	0.39
SCH4p5	1.03	1.09 (51)	0.46	1.20 (4)	4.95 (9)	16.6	17.5	1.08 (43)	−19.09	0.86	1.10	0.07	0.57
SCH4p0	1.00	1.03 (51)	0.38	1.16 (4)	4.23 (9)	16.5	17.3	9.01 (42)	−18.88	0.84	1.24	0.11	0.74
SCH3p5	0.98	9.71 (50)	0.30	1.14 (4)	3.50 (9)	16.4	16.5	7.34 (42)	−18.62	0.81	1.38	0.16	0.91
SCH3p0	0.95	9.19 (50)	0.23	1.11 (4)	2.73 (9)	16.5	15.2	5.76 (42)	−18.30	0.80	1.47	0.22	1.07
SCH2p5	0.93	8.67 (50)	0.17	1.08 (4)	2.08 (9)	16.4	14.9	4.36 (42)	−17.86	0.80	1.60	0.39	1.22
SCH2p0	0.90	8.14 (50)	0.12	1.05 (4)	1.52 (9)	15.9	14.6	3.17 (42)	−17.27	0.85	1.64	0.67	1.31
SCH1p5	0.88	7.59 (50)	0.08	1.02 (4)	1.09 (9)	15.4	13.4	2.26 (42)	−16.64	0.98	1.52	0.89	1.34

Notes: Numbers in parenthesis correspond to powers of ten. The ^{56}Ni mass corresponds to $t \approx 0$, and $v_{99}(^{56}{\rm Ni})$ is the velocity of the ejecta shell that bounds 99% of the total ^{56}Ni mass. $\dot{e}_{\rm decay}$ is the specific heating rate at bolometric maximum, corresponding to the instantaneous rate of decay energy actually deposited in the ejecta at this time ($L_{\rm decay}$) divided by the total mass ($M_{\rm tot}$). The last two columns give the $B-V$ colour at B-band maximum and 15 days later.

(Pinto & Eastman 2000). However, most theoretical studies of the WLR have either focused exclusively on Chandrasekhar-mass ($M_{\rm Ch}$) progenitors (e.g., Pinto & Eastman 2001; Mazzali et al. 2001; Höflich et al. 2002; Kasen & Woosley 2007), or excluded sub-$M_{\rm Ch}$ double-detonation models based on their apparent colour mismatch (see, e.g., Hoeflich et al. 1996). A generic problem of these sub-$M_{\rm Ch}$ models resides in the composition of the detonated He shell, which is needed to trigger a secondary detonation in the carbon-oxygen (C-O) core. The synthesis of ^{56}Ni and other IGEs in this external shell causes discrepant colours and spectra at early times (Nugent et al. 1997; Kromer et al. 2010). Nonetheless, Sim et al. (2010) have shown that pure central detonations in single sub-$M_{\rm Ch}$ WDs without an outer He shell are able to reproduce the overall trend of the observed WLR, although it is still unclear whether sub-$M_{\rm Ch}$ models fare better than the standard $M_{\rm Ch}$ scenario, in particular for low-luminosity SNe Ia. However, observational studies have shown that the narrow light curves of fast-declining SNe Ia likely result from sub-$M_{\rm Ch}$ ejecta, and that the WLR is naturally explained as a relation between ejected mass and ^{56}Ni mass (Scalzo et al. 2014a,b).

While the WLR imposes very strict constraints on SN Ia models, its reproduction by no means guarantees a high fidelity to observed events (see, e.g., Blondin et al. 2011). Moreover, the emphasis on the importance of the ionization balance in SN Ia ejecta to explain the WLR highlights the need for an accurate determination of the atomic level populations via a solution to the statistical equilibrium equations, i.e., a fully non-local-thermodynamic equilibrium (non-LTE) solution to the radiative transfer problem, often approximated in previous studies. Here we present 1D non-LTE time-dependent radiative transfer simulations of sub-$M_{\rm Ch}$ models for SNe Ia (Section 2), performed using the CMFGEN radiative-transfer code (Hillier & Dessart 2012).

To better illustrate the impact of a low ejecta mass on the radiative display, we confront these sub-$M_{\rm Ch}$ models to our previously-published $M_{\rm Ch}$ models, which include "standard" $M_{\rm Ch}$ delayed-detonations (DDC series; Blondin et al. 2013) and pulsational $M_{\rm Ch}$ delayed-detonations (PDDEL series; Dessart et al. 2014b). Despite the one-dimensional treatment of the explosion, these $M_{\rm Ch}$ models were found to capture the most salient features of more elaborate multi-dimensional simulations, in particular the asymptotic kinetic energy and chemical stratification (see, e.g., Seitenzahl et al. 2013). More importantly, they provided an excellent match to the observed

properties of both normal and low-luminosity SNe Ia at maximum light (Blondin et al. 2013), and to the spectral evolution of normal events out to $\lesssim$ 100 d past explosion (SN 2002bo, Blondin et al. 2015; SN 2005cf, Dessart et al. 2014c; SN 2011fe, Dessart et al. 2014b).

We start by analyzing the bolometric evolution of the sub-$M_{\rm Ch}$ models, highlighting the differences in rise time and post-maximum decline compared to $M_{\rm Ch}$ models at a given peak luminosity, i.e., similar ^{56}Ni mass but different WD mass, $M_{\rm tot}$ (Section 3). We then discuss the impact of a sub-$M_{\rm Ch}$ ejecta on the maximum-light $B-V$ colour (Section 4), and on its post-maximum evolution for low-luminosity SNe Ia (Section 5). Last, we assess the merits of sub-$M_{\rm Ch}$ progenitors in reproducing the observed WLR all the way to the faint end (Section 6). We discuss possible progenitor scenarios leading to the detonation of a sub-$M_{\rm Ch}$ WD in Section 7, followed by our conclusions.

2 SUB-CHANDRASEKHAR-MASS MODELS

The sub-$M_{\rm Ch}$ models studied here correspond to pure central detonations of WDs with a mass ranging between 0.88 M$_\odot$ and 1.15 M$_\odot$ (Table 1). As such they are similar to the sub-$M_{\rm Ch}$ models of Sim et al. (2010), albeit with a different numerical treatment and radiative-transfer post-processing (see below). The initial WD is assumed to be in hydrostatic equilibrium, and is composed of equal amounts of ^{12}C and ^{16}O by mass, with traces of ^{22}Ne and solar composition for all other isotopes. Importantly, we do not consider the presence of an external He shell, required in the double-detonation scenario to trigger a detonation in the C-O core. Despite the artificial nature of this setup, the models are nonetheless intrinsically coherent and enable us to qualitatively assess the impact of a lower ejecta mass on the radiative display. The 1D hydrodynamical treatment of the explosion phase is analogous to that used in our previous SN Ia studies based on $M_{\rm Ch}$ delayed-detonation models (see Blondin et al. 2013, their section 2). The calculation is carried out until the ejecta mass shells reach a ballistic regime (homologous expansion), less than $\sim$ 20 s past explosion. We smooth sharp variations in the composition and density profiles of the hydrodynamical input through convolution with a Gaussian kernel of width $\sigma = 800\,{\rm km\,s^{-1}}$ (see also Blondin et al. 2015).

One important difference is the absence of an initial deflagration phase, required to pre-expand the WD in $M_{\rm Ch}$ models and hence synthesize intermediate-mass elements during the secondary detonation phase. In sub-$M_{\rm Ch}$ models the burning can proceed directly in the form of a detonation wave, since the lower WD density ensures the burning will be incomplete in the outer ejecta layers with no prior pre-expansion. As a result, the initial WD structure sets the density at which the C-O fuel is burned, which is lower for lower WD masses. In particular, the amount of ^{56}Ni synthesized in the explosion is directly proportional to the WD mass, as is the asymptotic kinetic energy (see Table 1). In our sub-$M_{\rm Ch}$ model series (SCH), the initial range of WD masses (0.88–1.15 M$_\odot$) translates into a ^{56}Ni yield between 0.08 M$_\odot$ and 0.84 M$_\odot$.

The lower WD density also limits the production of neutron-rich stable isotopes of IGEs (e.g., ^{54}Fe, ^{58}Ni) in the inner ejecta, while these are more abundantly produced during the deflagration phase of $M_{\rm Ch}$ models. In the outer ejecta layers, however, the burning proceeds at similar densities in both the sub-$M_{\rm Ch}$ and $M_{\rm Ch}$ models considered here, resulting in similar abundance profiles. At a given ^{56}Ni yield, the sub-$M_{\rm Ch}$ models can thus be considered as low-mass analogs of the $M_{\rm Ch}$ models when discussing their radiative properties at early times, including the maximum-light phase discussed in the present paper.

The long-term evolution is computed with the 1D, time-dependent, non-LTE radiative-transfer code CMFGEN (Hillier & Dessart 2012; Dessart et al. 2014c), which includes the treatment of non-local energy deposition and non-thermal processes (e.g., Dessart et al. 2014a). Apart from the two-step ^{56}Ni$\rightarrow^{56}$Co$\rightarrow^{56}$Fe decay chain, we treat eight additional two-step decay chains associated with ^{37}K, ^{44}Ti, ^{48}Cr, ^{49}Cr, ^{51}Mn, ^{52}Fe, ^{55}Co, ^{57}Ni, and a further six one-step decay chains associated with ^{41}Ar, ^{42}K, ^{43}K, ^{43}Sc, ^{47}Sc, ^{61}Co (see Dessart et al. 2014c). All atom/ion level populations are determined explicitly through a solution of the time-dependent statistical equilibrium equations, which are coupled to the energy and radiative-transfer equations. We consider the following ions: C I–III, O I–III, Ne I–III, Na I, Mg II–III, Al II–III, Si II–IV, S II–IV, Ar I–III, Ca II–IV, Sc II–III, Ti II–III, Cr II–IV, Mn II–III, Fe I–VII, Co II–VII, and Ni II–VII. The number of levels considered for each ion is given in Appendix A, Table A1. We assume a constant effective Doppler width (including both thermal and turbulent velocities) of 50 km s^{-1} for our line-absorption profiles. While this value largely overestimates the true effective Doppler width (likely a few km s^{-1} at most) and hence the ejecta opacity, we have run extensive tests imposing an effective Doppler width of 10 km s^{-1} and found a negligible impact (at the few per cent level) on the predicted rise times and post-maximum decline rates. The output of such calculations are light curves and spectra that can be directly confronted to SN Ia observations. Our assumption of spherical symmetry allows for the most elaborate radiative-transfer treatment to date of such sub-$M_{\rm Ch}$ models.

In what follows we focus on the properties most relevant to the WLR, while the full SCH model series will be presented in more detail in a forthcoming paper.

3 BOLOMETRIC RISE AND POST-MAXIMUM DECLINE

Pinto & Eastman (2000) have emphasized the impact of the total mass[1] on the bolometric light curves of SNe Ia, through its effect on the ejecta density and γ-ray escape. A decrease in $M_{\rm tot}$ results in a lower column depth which favours a more rapid release of radiation at early times and an enhanced γ-ray escape fraction past maximum light, leading to a shorter rise time and a faster post-maximum decline. This is indeed the case for the sub-$M_{\rm Ch}$ models presented here, which display systematically shorter bolometric rise times than the $M_{\rm Ch}$ models for a given ^{56}Ni mass (Fig. 1, top panel).

Due to the shorter rise time, the instantaneous rate of energy deposition by radioactive decays ($L_{\rm decay}$) at maximum light is larger (as is the peak luminosity, $L_{\rm bol}$), resulting in a more efficient heating of the ejecta compared to a $M_{\rm Ch}$ model with the same ^{56}Ni mass. The lower $M_{\rm tot}$ exacerbates this effect, as the *specific* heating rate at maximum light ($\equiv L_{\rm decay}/M_{\rm tot}$, noted $\dot{e}_{\rm decay}$ in Table 1) is even larger. This latter parameter is key in explaining the bluer maximum-light colours of the sub-$M_{\rm Ch}$ models (see Section 4).

Moreover, all of the sub-$M_{\rm Ch}$ models have a bolometric decline rate $\Delta M_{15}({\rm bol}) \geqslant 0.80$ mag (and up to 0.98 mag), where the $M_{\rm Ch}$ models are confined to smaller values (0.54–0.76 mag; see Fig. 1,

[1] In this paper we only consider explosions that completely unbind the WD, hence the ejecta mass is equal to the WD mass.

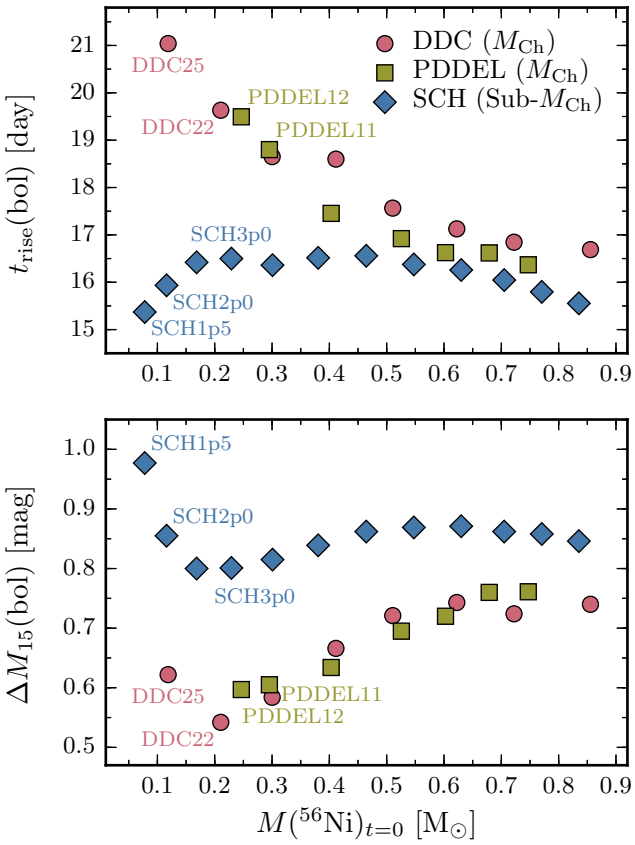

Figure 1. Bolometric rise time (top) and decline-rate ΔM_{15}(bol) (bottom) versus ^{56}Ni mass for the $M_{\rm Ch}$ (DDC series, circles; PDDEL series, squares) and sub-$M_{\rm Ch}$ models (diamonds).

bottom panel). This larger bolometric decline for the sub-$M_{\rm Ch}$ models will naturally affect all photometric bands, including the B-band on which the WLR is based (Section 6).

That said, both the $M_{\rm Ch}$ and sub-$M_{\rm Ch}$ models share a weak dependence of their post-maximum bolometric decline rate on the ^{56}Ni mass: the variation in ΔM_{15}(bol) is less than ~ 0.2 mag across a factor ~7–10 variation in ^{56}Ni mass. When excluding the faintest sub-$M_{\rm Ch}$ model (SCH1p5), the difference in ΔM_{15}(bol) drops to a mere 0.07 mag for the SCH series. This contrasts with the far stronger dependence of the post-maximum B-band decline rate $\Delta M_{15}(B)$ on ^{56}Ni mass (and hence peak luminosity; see Table 1), and lends support to the interpretation of the WLR as a colour effect as opposed to an increase of the diffusion time with ^{56}Ni mass (see Kasen & Woosley 2007).

In fact, the bolometric evolution more naturally follows an opposite trend to the (B-band) WLR, the more luminous models declining more rapidly (this is especially true in the ^{56}Ni mass range 0.2–0.6 M$_\odot$; see Fig. 1). The bolometric decline rate is related to the magnitude and rate of change of the γ-ray escape fraction past maximum light, which is larger for higher ^{56}Ni mass (see Stritzinger et al. 2006). This is in part due to the larger outward extent of the ^{56}Ni distribution (see the $v_{99}(^{56}{\rm Ni})$ column in Table 1) which favours the earlier and more rapid escape of γ-rays, thereby limiting the amount of decay energy actually deposited in the ejecta (see also Pinto & Eastman 2001). This effect is modulated by the release of stored radiation past maximum light, which leads to a secondary bolometric maximum whose timing can affect the value of ΔM_{15}(bol).

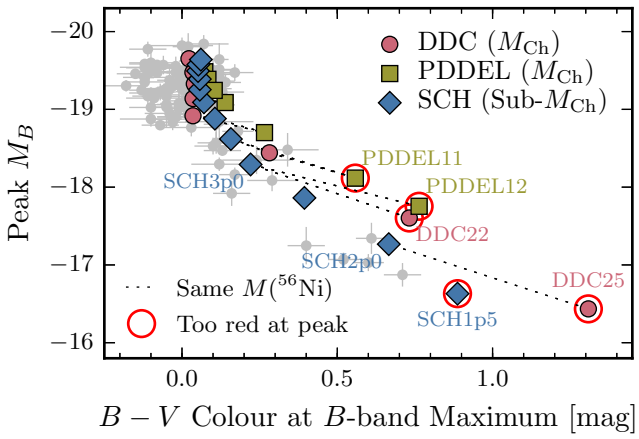

Figure 2. Peak B-band magnitude versus $B-V$ colour at B-band maximum for the $M_{\rm Ch}$ (DDC series, circles; PDDEL series, squares) and sub-$M_{\rm Ch}$ models (diamonds). Models with a similar ^{56}Ni mass (within ± 0.02 M$_\odot$) are connected with a dotted line. Also shown are measurements taken from Hicken et al. (2009) [grey points]. Models that have a too red $B-V$ colour at B-band maximum are highlighted with a red circle.

4 MAXIMUM-LIGHT COLOURS

Type Ia supernovae obey a strong relation between their peak M_B and their $B-V$ colour at maximum light, brighter events displaying bluer colours (e.g., Tripp 1998). This relation simply reflects the larger magnitude of decay heating from ^{56}Ni for more luminous events, and holds for both $M_{\rm Ch}$ and sub-$M_{\rm Ch}$ models (Fig. 2).

Nonetheless, one would expect the greater *specific* heating rate ($\dot{e}_{\rm decay}$; see previous section) for the sub-$M_{\rm Ch}$ models at a given ^{56}Ni mass to result in even bluer colours. As seen in Fig. 2, this effect is present and more pronounced at the faint end (up to ~ 0.6 mag bluer $B-V$ colour at a given ^{56}Ni mass), where the relative difference in $\dot{e}_{\rm decay}$ is largest (see Table 1). In contrast, all models brighter than $M_B = -19$ mag at peak have very similar $B-V$ colours at maximum ($\lesssim 0.03$ mag standard deviation).

The sub-$M_{\rm Ch}$ models follow the observed relation all the way to the faint end (peak $M_B \gtrsim -17$ mag), while the $M_{\rm Ch}$ models are systematically too red at a given peak M_B. This is also the case for the least luminous sub-$M_{\rm Ch}$ model (SCH1p5), in which the ^{56}Ni mass is too low (< 0.08 M$_\odot$, where all the other models have $\gtrsim 0.12$ M$_\odot$ of ^{56}Ni; see Table 1) to efficiently heat the spectrum-formation layers at maximum light. In fact, the only model to have an even redder $B-V$ colour at maximum is the $M_{\rm Ch}$ model DDC25, which has the lowest specific heating rate of all ($\dot{e}_{\rm decay} < 10^9$ erg s^{-1} g^{-1}).

5 THE POST-MAXIMUM COLOUR EVOLUTION OF LOW-LUMINOSITY SNe Ia

We focus on three models with similar ^{56}Ni mass (within ± 0.02 M$_\odot$ of 0.23 M$_\odot$) to better illustrate the impact of $M_{\rm tot}$ on the post-maximum colour evolution of low-luminosity SNe Ia: the standard $M_{\rm Ch}$ delayed-detonation model DDC22, the pulsational $M_{\rm Ch}$ delayed-detonation model PDDEL12, and the sub-$M_{\rm Ch}$ model SCH3p0, corresponding to the pure central detonation of a 0.95 M$_\odot$ C-O WD. Their B-band light curves (normalized to the same peak magnitude) and $B-V$ colour evolution is shown in Fig. 3. One clearly notes the faster evolution of the B-band light curve for the sub-$M_{\rm Ch}$ model (in part due to the faster bolometric evolution; see Fig. 3 inset), with a ~ 2 d shorter rise time and a > 0.3 mag larger

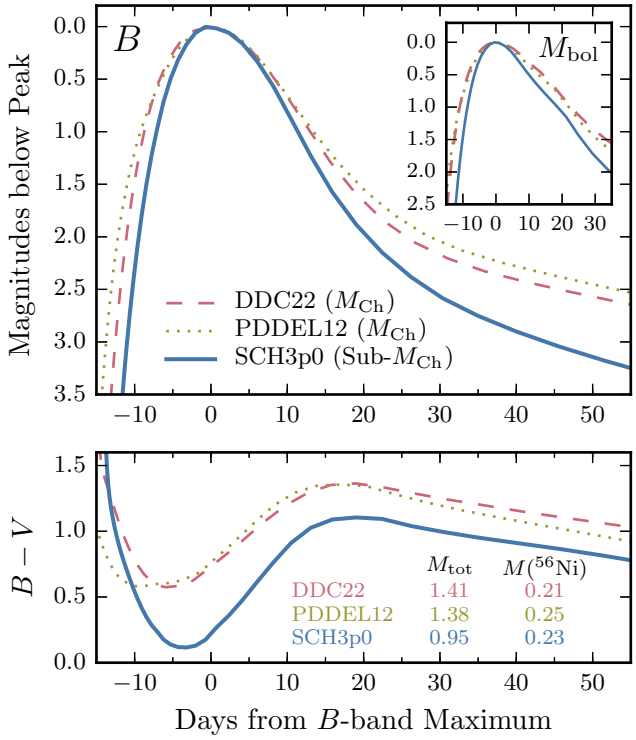

Figure 3. Normalized B-band light curves (top) and $B-V$ colour evolution (bottom) for the standard $M_{\rm Ch}$ delayed-detonation model DDC22 (dashed line), the pulsational $M_{\rm Ch}$ delayed-detonation model PDDEL12 (dotted line), and the sub-$M_{\rm Ch}$ model SCH3p0 ($M_{\rm tot}$ = 0.95 M$_\odot$; solid line), all of which have a similar ^{56}Ni mass of 0.23 ± 0.02 M$_\odot$. The inset shows the normalized bolometric light curves, where the time axis now corresponds to days from bolometric maximum.

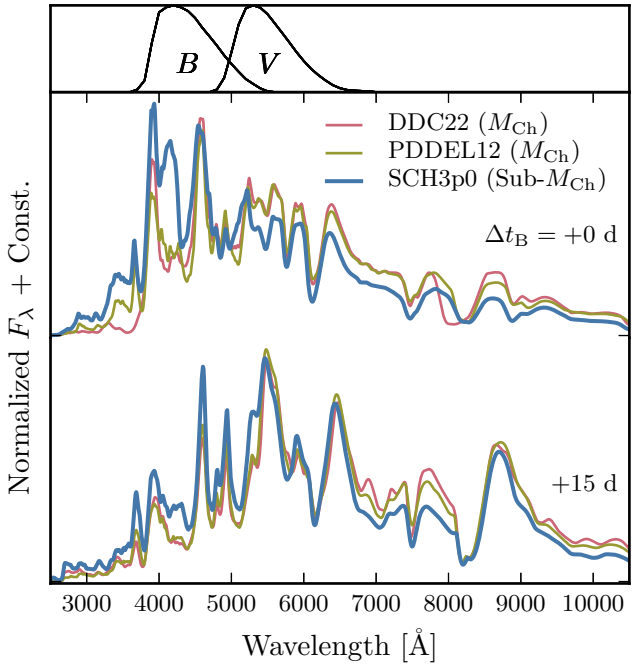

Figure 4. Optical spectra at B-band maximum and 15 days later, for the standard $M_{\rm Ch}$ delayed-detonation model DDC22 (red line), the pulsational $M_{\rm Ch}$ delayed-detonation model PDDEL12 (yellow line), and the sub-$M_{\rm Ch}$ model SCH3p0 ($M_{\rm tot}$ = 0.95 M$_\odot$; blue line), all of which have a similar ^{56}Ni mass of 0.23 ± 0.02 M$_\odot$. The spectra have been normalized to their mean flux in the range 3000–10000 Å. The upper panel shows the normalized transmission curves for the B and V filters.

$\Delta M_{15}(B)$ [see Table 1], accompanied by a faster evolution of the $B-V$ colour around maximum light. This results in a gradual decrease in the difference in $B-V$ colour compared to the $M_{\rm Ch}$ models, from > 0.5 mag at B-band maximum to < 0.3 mag 15 days later.

The greater specific heating rate of the sub-$M_{\rm Ch}$ model ($\dot{e}_{\rm decay}$; see Section 3) results in a relatively modest increase of the temperature in the spectrum-formation region at maximum light compared to the $M_{\rm Ch}$ models (on the order of 10–15%). Combined with the lower ejecta density, this slightly larger temperature is nonetheless sufficient to induce a change in the mean ionization state of the gas, enhancing the III/II ionization ratio of IGEs (Sc, Ti, Cr, Fe, and Co) that would otherwise effectively block the flux in the B-band and emit in redder bands in their once-ionized state (especially Fe II; see Appendix B).

The bluer $B-V$ colour of the sub-$M_{\rm Ch}$ model thus results both from an overall shift of the SED to the blue (akin to a purely thermal effect) and a modulation of line-blanketing from changes in ionization. Both effects are clearly visible in the maximum-light spectra shown in Fig. 4. By 15 days past B-band maximum, the temperature in the spectrum-formation region of the sub-$M_{\rm Ch}$ model has decreased sufficiently to enhance the absorption by singly-ionized IGEs to a level comparable to that in the $M_{\rm Ch}$ models. The differences in B-band flux as well as in the overall SED shape are greatly reduced at this phase, although the sub-$M_{\rm Ch}$ model remains slightly bluer, thereby limiting the B-band post-maximum decline rate.

6 THE WIDTH-LUMINOSITY RELATION

The WLR for the $M_{\rm Ch}$ and sub-$M_{\rm Ch}$ models is shown in Fig. 5. At the bright end (peak $M_B \lesssim -18.5$ mag), both $M_{\rm Ch}$ and sub-$M_{\rm Ch}$ models follow the observed WLR (grey data points in Fig. 5), albeit with slightly steeper slopes (similar for the DDC and SCH series, and somewhat shallower for the PDD series). At the faint end (peak $M_B \gtrsim -18.5$ mag), the $M_{\rm Ch}$ models display a turnover to an *anti* WLR, reaching a maximum $\Delta M_{15}(B)$ value of ∼ 1.4 mag (DDC series) and ∼ 1.3 mag (PDDEL series). These models correspond to the same ones that have a too red $B-V$ colour at maximum light in Fig. 2 (highlighted with red circles in both figures), due to the less efficient heating of the spectrum-formation region from the lower $\dot{e}_{\rm decay}$ (Section 4). Combined with a modest post-maximum evolution of their $B-V$ colour, the resulting B-band decline rate is then too low for the $M_{\rm Ch}$ models to reproduce the faint end of the WLR despite their low luminosity.

In the sub-$M_{\rm Ch}$ models, the more rapid colour evolution around maximum light combined with a larger bolometric decline rate result in a higher $\Delta M_{15}(B)$ for the same ^{56}Ni mass. Consequently, only the sub-$M_{\rm Ch}$ models extend beyond $\Delta M_{15}(B)$ = 1.4 mag. This confirms the WD mass as an essential parameter in producing rapidly-declining SNe Ia at the faint end of the WLR. In particular, the sub-$M_{\rm Ch}$ model SCH2p0 ($M_{\rm tot}$ = 0.90 M$_\odot$) has a ∼ 0.6 mag larger $\Delta M_{15}(B)$ value than the $M_{\rm Ch}$ model with the same ^{56}Ni mass, DDC25 ($M(^{56}{\rm Ni})$ = 0.12 M$_\odot$ for both).

We note, however, that the sub-$M_{\rm Ch}$ models also transition to an anti-WLR, albeit at much fainter magnitudes (peak $M_B \gtrsim -17$ mag), and that they fail to reach the highest observed $\Delta M_{15}(B)$ values. We speculate that small variations in the $M(^{56}{\rm Ni})/M_{\rm tot}$ ratio or in the ^{56}Ni distribution within the ejecta (due to explosion

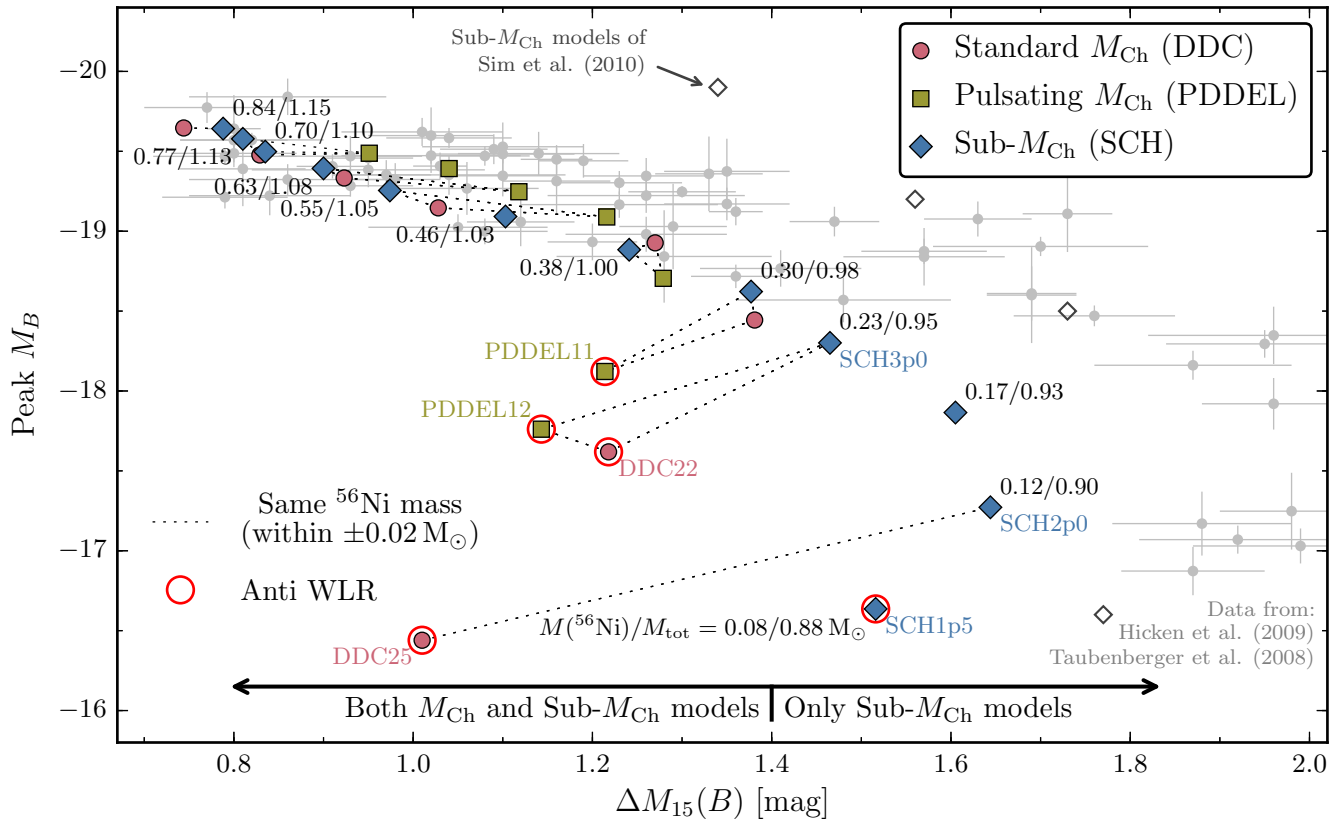

Figure 5. Width-luminosity relation for the $M_{\rm Ch}$ (DDC series, circles; PDDEL series, squares) and sub-$M_{\rm Ch}$ models (filled diamonds; the numbers associated with each symbol corresponds to the ^{56}Ni and progenitor WD mass, respectively). Models with a similar ^{56}Ni mass (within ±0.02 M$_\odot$) are connected with a dotted line. Also shown are the pure C-O sub-$M_{\rm Ch}$ models of Sim et al. (2010) [open diamonds], as well as measurements taken from Hicken et al. (2009) and Taubenberger et al. (2008) [grey points]. Models that have transitioned to an *anti* WLR are highlighted with a red circle. These correspond to the same models that have a too red $B-V$ colour at maximum light in Fig. 2. Only the sub-$M_{\rm Ch}$ models yield B-band light curves with a decline-rate $\Delta M_{15}(B) > 1.4$ mag.

asymmetries or large-scale mixing) could enhance the rate of γ-ray escape and lead to a better agreement with the data in this respect. We will discuss this in more detail in a companion paper in which we compare the SCH2p0 model to the low-luminosity SN 1999by.

The sub-$M_{\rm Ch}$ models of Sim et al. (2010) yield systematically larger $\Delta M_{15}(B)$ values compared to our SCH models at a given peak M_B, by up to ~ 0.6 mag for their two most luminous models and ~ 0.3 mag for their two least luminous models (Fig. 5). Their most luminous model ($M(^{56}{\rm Ni})/{\rm M_{tot}} = 0.81/1.15$ M$_\odot$, similar to our SCH7p0 model) declines too slowly for its luminosity, with $\Delta M_{15}(B) \approx 1.3$ mag for a peak $M_B \approx -20$, where SNe Ia of comparable luminosity (and our SCH7p0 model) have $\Delta M_{15}(B) \approx 0.8$ mag. Their least luminous model, however, is in better agreement with the observed WLR, with $\Delta M_{15}(B) \approx 1.8$ mag where our SCH1p5 model only has $\Delta M_{15}(B) \approx 1.5$ mag for the same peak $M_B \approx -16.6$. Differences in the nucleosynthetic post-processing of the explosion models and in the radiative-transfer treatment are the likely causes of these offsets (Sim, priv. comm.).

As was the case for the bolometric light curves (Section 3), the faster B-band post-maximum decline of the sub-$M_{\rm Ch}$ models is associated with a shorter B-band rise time, as observed for low-luminosity SNe Ia (Ganeshalingam et al. 2011). To match the current practice of observers, the time reference is set to maximum light. Studies of the WLR thus ignore the scatter in rise times for SNe Ia with different peak M_B. While determining the precise time of explosion is observationally complicated, the recent examples of SN 2011fe (Nugent et al. 2011), SN 2013dy (Zheng et al. 2013), and three SN Ia candidates discovered during the Kepler mission (Olling et al. 2015) illustrate the potential of high-cadence searches to constrain the rise time. Future studies of the WLR will then need to consider the pre-maximum rise as well as the post-maximum decline when distinguishing between fast and slow light-curve evolution.

7 DISCUSSION AND CONCLUSIONS

The predicted observational signatures of pure central detonations in sub-$M_{\rm Ch}$ WDs corroborate a number of distinctive properties of low-luminosity SNe Ia. At a given ^{56}Ni mass, the lower ejecta mass compared to $M_{\rm Ch}$ models results in a faster bolometric evolution around maximum light, which affects all photometric bands. Furthermore, the larger $M(^{56}{\rm Ni})/M_{\rm tot}$ ratio leads to a bluer $B-V$ colour at maximum light and a higher post-maximum B-band decline rate, $\Delta M_{15}(B)$, in better agreement with the observed WLR. Conversely, the lower *specific* heating rate in the $M_{\rm Ch}$ models considered here results in a $B-V$ colour at maximum that is too red compared to observations (through excess absorption by singly-ionized IGEs and weaker emission in the blue), and hence a more modest post-maximum colour evolution that imposes an upper limit on the $\Delta M_{15}(B)$ value.

Even then, the sub-$M_{\rm Ch}$ models fail to match the fastest decline rates observed for low-luminosity, 91bg-like SNe Ia. Variations in

the $M(^{56}\mathrm{Ni})/M_{\rm tot}$ ratio or in the ^{56}Ni distribution within the ejecta could enhance the rate of γ-ray escape and result in a more efficient cooling of the spectrum-formation region at these phases. Sim et al. (2010) also find that a modest change in the initial WD composition (replacing 7.5% by mass of ^{12}C with ^{22}Ne) has a non-negligible impact on the resulting $\Delta M_{15}(B)$ value. We note that a similar $M(^{56}\mathrm{Ni})/M_{\rm tot}$ ratio as our low-luminosity sub-$M_{\rm Ch}$ models can in principle be achieved in the context of $M_{\rm Ch}$ models if the explosion is too weak to completely unbind the WD, leaving behind a bound remnant (see Fink et al. 2014).

The sub-$M_{\rm Ch}$ (and $M_{\rm Ch}$) models studied here remain somewhat artificial for genuine quantitative predictions to be made, yet the level of sophistication enabled by the 1D treatment of the radiative transfer enables us to qualitatively assess the impact of a lower ejecta mass on the ionization balance for a given ^{56}Ni mass, which is crucial in explaining the observed WLR. Ultimately, our results will need to be confirmed by more realistic, multi-dimensional models, although radiative-transfer simulations with the same level of sophistication as ours are currently not feasible in 3D (see, e.g., Sim et al. 2013).

But do such low-mass explosions occur in Nature? Detonations of sub-$M_{\rm Ch}$ WDs require an external trigger, usually via thermal instabilities in a layer of accreted He (double detonation mechanism; see, e.g., Woosley & Weaver 1994). This layer can detonate at a lower mass than previously thought (Bildsten et al. 2007), but the resulting IGEs synthesized at high velocities cause discrepant colours and spectra at early times (Kromer et al. 2010). More recent calculations by Shen & Moore (2014), however, show that a detonation in a 0.005 $\mathrm{M}_\odot$ He shell on a 1.0 $\mathrm{M}_\odot$ WD only produces ^{28}Si and ^{4}He, and that significant ^{44}Ti/^{48}Cr production only occurs for shells more massive than $\sim 0.01\,\mathrm{M}_\odot$. Double detonations thus remain an attractive scenario for fast-declining SNe Ia for which empirical determinations of the ejecta mass indicate sub-$M_{\rm Ch}$ progenitors (Scalzo et al. 2014a,b).

Likewise, He-ignited violent mergers (Pakmor et al. 2013), where the dynamical detonation of $0.01\mathrm{M}_\odot$ of He is sufficient to trigger a detonation in the C-O core, also synthesize very little IGEs in the outer layers ($\sim 10^{-8}\,\mathrm{M}_\odot$). In particular, Pakmor et al. (2013) argue that low-luminosity SNe Ia result from the violent merger of a C-O+He WD system, which is less massive (and hence results in a more rapid light-curve evolution) than double C-O WD mergers. The predicted rate of such systems can in principle account for the observed SN Ia rate (Ruiter et al. 2011), and their long delay times would corroborate the association of low-luminosity SNe Ia with older stellar populations (e.g., Howell 2001).

Another possibility, suggested by van Kerkwijk et al. (2010), involves the merger of two low-mass WDs whose combined mass is less than the Chandrasekhar limit (a $0.6 + 0.6\,\mathrm{M}_\odot$ merger in their paper). The explosion does not occur during the merger event, but at a later time via compressional heating through accretion of the thick disk from the merger remnant (see Lorén-Aguilar et al. 2009). However, this scenario is unlikely to hold for a combined merger mass $\lesssim 1.2\,\mathrm{M}_\odot$, given the high temperature and density conditions required to ignite carbon (van Kerkwijk, priv. comm.), and hence would fail to reproduce the fast-declining SNe Ia at the faint end of the WLR, which we argue result from ejecta masses $\lesssim 1\,\mathrm{M}_\odot$. In this respect, head-on collisions of two $0.5\,\mathrm{M}_\odot$ WDs represent an interesting alternative: Kushnir et al. (2013) find that such a model yields $0.11\,\mathrm{M}_\odot$ of ^{56}Ni, comparable to our SCH2p0 model. However, most studies of this progenitor channel conclude that WD collisions can account for at most a few per cent of the observed SN Ia rate (see, e.g., Papish & Perets 2016).

Regardless of the precise ignition mechanism, the results presented in this paper strongly suggest that explosions of sub-$M_{\rm Ch}$ WDs are a viable scenario for fast-declining SNe Ia at the faint end of the WLR, whose colours cannot be reproduced by $M_{\rm Ch}$ models. In several upcoming companion papers we will present an in-depth study of the sub-$M_{\rm Ch}$ model SCH2p0 compared to the low-luminosity SN 1999by, and explore more generally the feasibility of such sub-$M_{\rm Ch}$ models to reproduce the observed properties of more luminous events, to address the question of multiple progenitor channels for Type Ia supernovae.

ACKNOWLEDGEMENTS

SB acknowledges useful discussions with Inma Domínguez, Stuart Sim and Marten van Kerkwijk. Part of this work was realized during a one-month visit of SB to ESO as part of the ESO Scientific Visitor Programme. LD and SB acknowledge financial support from the Programme National de Physique Stellaire (PNPS) of CNRS/INSU, France. DJH acknowledges support from STScI theory grant HST-AR-12640.01, and NASA theory grant NNX14AB41G. This work was granted access to the HPC resources of CINES under the allocation c2014046608 made by GENCI (Grand Equipement National de Calcul Intensif). This work also utilized computing resources of the mesocentre SIGAMM, hosted by the Observatoire de la Côte d'Azur, Nice, France.

REFERENCES

Becker S. R., Butler K., 1992, A&A, 265, 647
Becker S. R., Butler K., 1995a, A&A, 294, 215
Becker S. R., Butler K., 1995b, A&A, 301, 187
Berrington K. A., Burke P. G., Dufton P. L., Kingston A. E., 1985, Atomic Data and Nuclear Data Tables, 33, 195
Bildsten L., Shen K. J., Weinberg N. N., Nelemans G., 2007, ApJ, 662, L95
Blondin S., Kasen D., Röpke F. K., Kirshner R. P., Mandel K. S., 2011, MNRAS, 417, 1280
Blondin S., Dessart L., Hillier D. J., Khokhlov A. M., 2013, MNRAS, 429, 2127
Blondin S., Dessart L., Hillier D. J., 2015, MNRAS, 448, 2766
Contardo G., Leibundgut B., Vacca W. D., 2000, A&A, 359, 876
Dessart L., Hillier D. J., 2010, MNRAS, 405, 2141
Dessart L., Hillier D. J., Blondin S., Khokhlov A., 2014a, MNRAS, 439, 3114
Dessart L., Blondin S., Hillier D. J., Khokhlov A., 2014b, MNRAS, 441, 532
Dessart L., Hillier D. J., Blondin S., Khokhlov A., 2014c, MNRAS, 441, 3249
Fink M., et al., 2014, MNRAS, 438, 1762
Ganeshalingam M., Li W., Filippenko A. V., 2011, MNRAS, 416, 2607
Hicken M., et al., 2009, ApJ, 700, 331
Hillier D. J., Dessart L., 2012, MNRAS, 424, 252
Hillier D. J., Miller D. L., 1998, ApJ, 496, 407
Hoeflich P., Khokhlov A., Wheeler J. C., Phillips M. M., Suntzeff N. B., Hamuy M., 1996, ApJ, 472, L81
Höflich P., Gerardy C. L., Fesen R. A., Sakai S., 2002, ApJ, 568, 791
Howell D. A., 2001, ApJ, 554, L193
Hummer D. G., Berrington K. A., Eissner W., Pradhan A. K., Saraph H. E., Tully J. A., 1993, A&A, 279, 298
Kasen D., Woosley S. E., 2007, ApJ, 656, 661
Kingdon J. B., Ferland G. J., 1996, ApJS, 106, 205
Kromer M., Sim S. A., Fink M., Röpke F. K., Seitenzahl I. R., Hillebrandt W., 2010, ApJ, 719, 1067
Kurucz R. L., 2009, in Hubeny I., Stone J. M., MacGregor K., Werner K., eds, American Institute of Physics Conference Series Vol. 1171, American

Institute of Physics Conference Series. pp 43–51 (arXiv:0912.5371), doi:10.1063/1.3250087
Kushnir D., Katz B., Dong S., Livne E., Fernández R., 2013, ApJ, 778, L37
Lennon D. J., Burke V. M., 1994, A&AS, 103, 273
Lennon D. J., Dufton P. L., Hibbert A., Kingston A. E., 1985, ApJ, 294, 200
Lorén-Aguilar P., Isern J., García-Berro E., 2009, A&A, 500, 1193
Mazzali P. A., Nomoto K., Cappellaro E., Nakamura T., Umeda H., Iwamoto K., 2001, ApJ, 547, 988
Mendoza C., 1983, in D. R. Flower ed., IAU Symposium Vol. 103, Planetary Nebulae. pp 143–172
Nahar S. N., 1995, A&A, 293, 967
Nahar S. N., 2010, NORAD-Atomic-Data, http://www.astronomy.ohio-state.edu/~nahar/
Nugent P., Baron E., Branch D., Fisher A., Hauschildt P. H., 1997, ApJ, 485, 812
Nugent P. E., et al., 2011, Nature, 480, 344
Nussbaumer H., Storey P. J., 1983, A&A, 126, 75
Nussbaumer H., Storey P. J., 1984, A&AS, 56, 293
Olling R. P., et al., 2015, Nature, 521, 332
Pakmor R., Kromer M., Taubenberger S., Springel V., 2013, ApJ, 770, L8
Papish O., Perets H. B., 2016, ApJ, 822, 19
Perlmutter S., et al., 1999, ApJ, 517, 565
Phillips M. M., 1993, ApJ, 413, L105
Pinto P. A., Eastman R. G., 2000, ApJ, 530, 744
Pinto P. A., Eastman R. G., 2001, New Astronomy, 6, 307
Pskovskii I. P., 1977, Soviet Astronomy, 21, 675
Riess A. G., et al., 1998, AJ, 116, 1009
Ruiter A. J., Belczynski K., Sim S. A., Hillebrandt W., Fryer C. L., Fink M., Kromer M., 2011, MNRAS, 417, 408
Scalzo R., et al., 2014a, MNRAS, 440, 1498
Scalzo R. A., Ruiter A. J., Sim S. A., 2014b, MNRAS, 445, 2535
Seaton M. J., 1987, Journal of Physics B Atomic Molecular Physics, 20, 6363
Seitenzahl I. R., et al., 2013, MNRAS, 429, 1156
Shen K. J., Moore K., 2014, ApJ, 797, 46
Shine R. A., Linsky J. L., 1974, Sol. Phys., 39, 49
Sim S. A., Röpke F. K., Hillebrandt W., Kromer M., Pakmor R., Fink M., Ruiter A. J., Seitenzahl I. R., 2010, ApJ, 714, L52
Sim S. A., et al., 2013, MNRAS, 436, 333
Stritzinger M., Leibundgut B., Walch S., Contardo G., 2006, A&A, 450, 241
Taubenberger S., et al., 2008, MNRAS, 385, 75
Tayal S. S., 1997a, ApJS, 111, 459
Tayal S. S., 1997b, ApJ, 481, 550
Tripp R., 1998, A&A, 331, 815
Woosley S. E., Weaver T. A., 1994, ApJ, 423, 371
Zhang H. L., Pradhan A. K., 1995a, Journal of Physics B Atomic Molecular Physics, 28, 3403
Zhang H. L., Pradhan A. K., 1995b, A&A, 293, 953
Zhang H. L., Pradhan A. K., 1997, A&AS, 126, 373
Zheng W., et al., 2013, ApJ, 778, L15
van Kerkwijk M. H., Chang P., Justham S., 2010, ApJ, 722, L157

APPENDIX A: MODEL ATOMS

Table A1 gives the number of levels (both super-levels and full levels; see Hillier & Miller 1998 and Dessart & Hillier 2010 for details) for the model atoms used in the radiative-transfer calculations presented in this paper.

Oscillator strengths for CNO elements were originally taken from Nussbaumer & Storey (1983, 1984). These authors also provide transition probabilities to states in the ion continuum. The largest source of oscillator data is from Kurucz (2009)[2]; its principal advantage over many other sources (e.g., Opacity Project) is that LS coupling is not assumed. More recently, non-LS oscillator strengths have become available through the Iron Project (Hummer et al. 1993), and work done by the atomic-data group at Ohio State University (Nahar 2010). Other important sources of radiative data for Fe include Becker & Butler (1992, 1995a,b), Nahar (1995). Energy levels have generally been obtained from the National Institute of Standards and Technology. Collisional data is sparse, particularly for states far from the ground state. The principal source for collisional data among low lying states for a variety of species is the tabulation by Mendoza (1983); other sources include Berrington et al. (1985), Lennon et al. (1985), Lennon & Burke (1994), Shine & Linsky (1974), Tayal (1997a,b), Zhang & Pradhan (1995b; 1995a; 1997). Photoionization data is taken from the Opacity Project (Seaton 1987) and the Iron Project (Hummer et al. 1993). Unfortunately Ni and Co photoionization data is generally unavailable, and we have utilized crude approximations. Charge exchange cross-sections are from the tabulation by Kingdon & Ferland (1996).

[2] Data are available online at http://kurucz.harvard.edu

APPENDIX B: CONTRIBUTION OF INDIVIDUAL IONS TO THE TOTAL OPTICAL FLUX

Figure B1 reveals the contribution of individual ions (bottom panels) to the full optical synthetic spectra of the standard $M_{\rm Ch}$ delayed-detonation model DDC22, the pulsational $M_{\rm Ch}$ delayed-detonation model PDDEL12, and the sub-$M_{\rm Ch}$ model SCH3p0 ($M_{\rm tot} = 0.95\,{\rm M}_{\odot}$), all of which have a similar ^{56}Ni mass of $0.23 \pm 0.02\,{\rm M}_{\odot}$, at B-band maximum light and 15 days later. Only ions that impact the flux at the > 10 per cent level at either phase are shown.

This paper has been typeset from a TEX/LATEX file prepared by the author.

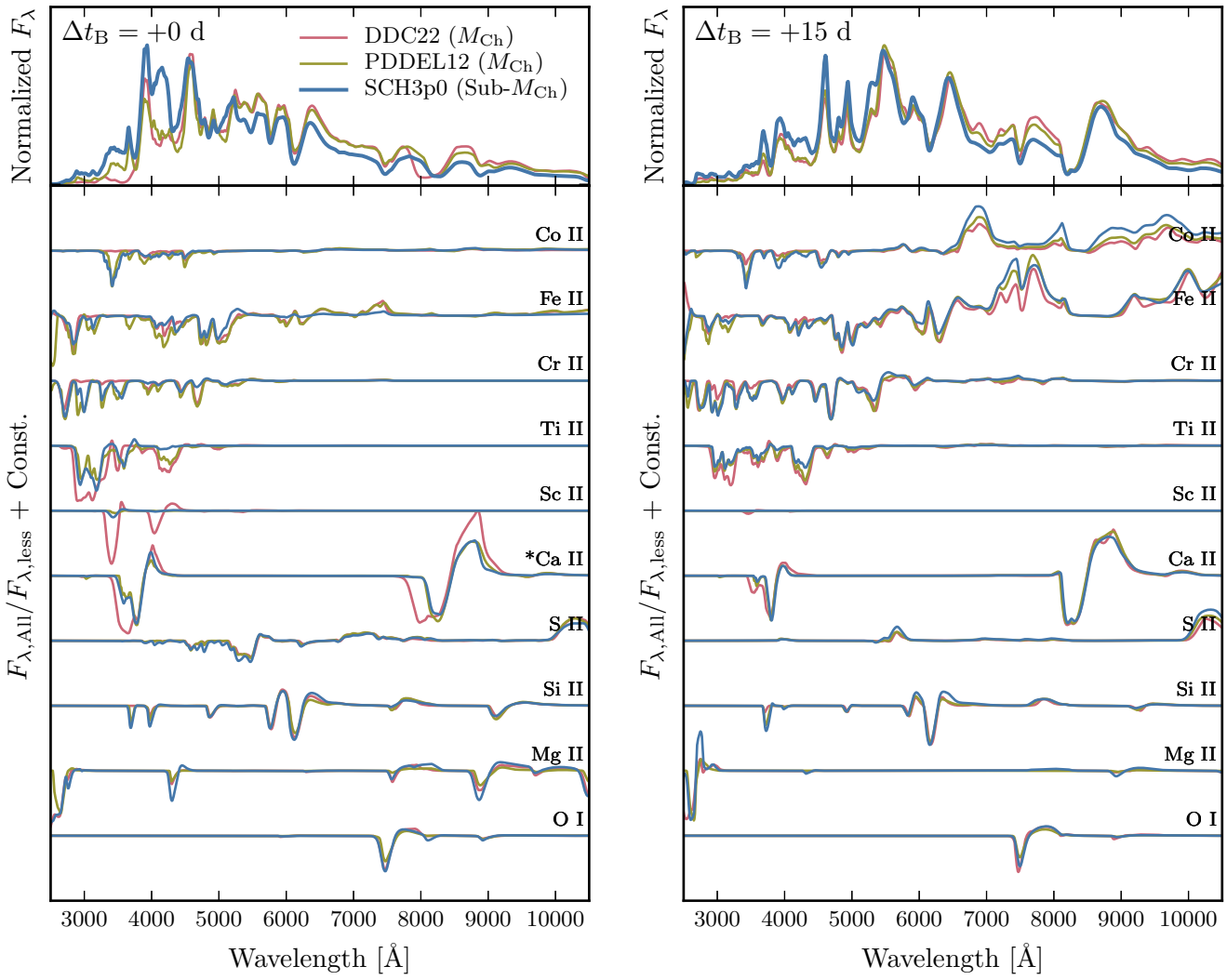

Figure B1. Contribution of individual ions (bottom panels) to the full optical synthetic spectra of the standard $M_{\rm Ch}$ delayed-detonation model DDC22 (red line), the pulsational $M_{\rm Ch}$ delayed-detonation model PDDEL12 (yellow line), and the sub-$M_{\rm Ch}$ model SCH3p0 ($M_{\rm tot}$ = 0.95 $M_\odot$; blue line), all of which have a similar ^{56}Ni mass of 0.23 ± 0.02 $M_\odot$, at B-band maximum light (left) and 15 days later (right). The spectra have been normalized to their mean flux in the range 3000–10000 Å. Only ions that impact the flux at the > 10 per cent level at either phase are shown. The Ca II ion spectra marked with a "*" have been scaled down for clarity.

Table A1. Summary of the model atoms used in our radiative-transfer calculations (see also Dessart & Hillier 2010). N_f refers to the number of full levels, N_s to the number of super levels, and N_{trans} to the corresponding number of bound-bound transitions. The last column refers to the upper level for each ion treated. Note that *n*w ^{2}W refers to a state with principal quantum number *n* (all *l* states combined into a single state), and spin 2.

Species	N_f	N_s	N_{trans}	Upper Level
C I	26	14	120	$2s2p^3\ ^3P^o$
C II	26	14	98	$2s^24d\ ^2D_{5/2}$
C III	112	62	906	$2s8f\ ^1F^o$
O I	101	38	743	$2s^22p^3(^4S^o)6f\ ^3F_2$
O II	143	63	1868	$2s^22p^2(^3P)5p\ ^2P^o_{3/2}$
O III	86	44	516	$2s2p^2(^4P)3p\ ^3P^o$
Ne I	139	70	1587	$2s^22p^5(^2P^o_{3/2})6d\ ^2[5/2]^o_3$
Ne II	91	22	1107	$2s^22p^4(^3P)4d\ ^2P_{3/2}$
Ne III	56	24	240	$2s^22p^3(^3S^o)4p\ ^5P$
Na I	71	22	1614	$30w\ ^2W$
Mg II	80	31	1993	$30w\ ^2W$
Mg III	99	31	775	$2p^57s\ ^1P^o$
Al II	44	26	171	$3s5d\ ^1D_2$
Al III	80	31	2011	$30w\ ^2W$
Si II	59	31	354	$3s^27g\ ^2G_{7/2}$
Si III	61	33	312	$3s5g\ ^3G_5$
Si IV	48	37	405	$10f\ ^2F^o$
S II	324	56	8464	$3s3p^3(^5S^o)4p\ ^6P$
S III	98	48	840	$3s3p^2(^2D)3d\ ^3P$
S IV	67	27	397	$3s3p(^3P^o)4p\ ^2D_{5/2}$
Ar I	110	56	1541	$3s^23p^5(^2P^o_{3/2})7p\ ^2[3/2]_2$
Ar II	415	134	20197	$3s^23p^4(^3P_1)7i\ ^2[6]_{11/2}$
Ar III	346	32	6901	$3s^23p^3(^2D^o)8s\ ^1D^o$
Ca II	77	21	1736	$3p^630w\ ^2W$
Ca III	40	16	108	$3s^23p^55s\ ^1P^o$
Ca IV	69	18	335	$3s3p^5(^3P^o)3d\ ^4D^o_{1/2}$
Sc II	85	38	979	$3p^63d4f\ ^1P^o_1$
Sc III	45	25	235	$7h\ ^2H^o_{11/2}$
Ti II	152	37	3134	$3d^2(^3F)5p\ ^4D^o_{7/2}$
Ti III	206	33	4735	$3d6f\ ^3H^o_6$
Cr II	196	28	4162	$3d^4(^3G)4p\ x^4G^o_{11/2}$
Cr III	145	30	2359	$3d^3(^2D_2)4p\ ^3D^o_3$
Cr IV	234	29	6354	$3d^2(^3P)5p\ ^4P^o_{5/2}$
Mn II	97	25	236	$3d^4(^5D)4s^2\ c^5D_4$
Mn III	175	30	3173	$3d^4(^3G)4p\ y^4H^o_{13/2}$
Fe I	136	44	1900	$3d^6(^5D)4s4p\ x^5F^o_3$
Fe II	827	275	44 831	$3d^5(^6S)4p^2(^3P)\ ^4P_{1/2}$
Fe III	698	83	36 807	$3d^5(^2H)4d^1K_7$
Fe IV	1000	100	72 223	$3d^4(^3G)4f\ ^4P^o_{5/2}$
Fe V	191	47	3977	$3d^3(^4F)4d\ ^5F_3$
Fe VI	433	44	14 103	$3p^5(^2P)3d^4(^1S)\ ^2P^o_{3/2}$
Fe VII	153	29	1753	$3p^5(^2P)3d^3(^2D)\ ^1P^o_1$
Co II	2747	136	593 559	$3d^7(^2D)6p\ ^3P^o_1$
Co III	3917	123	679 412	$3d^6(^3D)6d\ ^4P_{3/2}$
Co IV	314	37	9062	$3d^5(^2P)4p\ ^3P^o_1$
Co V	387	32	13 605	$3d^4(^3F)4d\ ^2H_{9/2}$
Co VI	323	28	9608	$3d^3(^2D)4d\ ^1S$
Co VII	319	31	9096	$3p^5(^2P)4d(^3F)\ ^2D^o_{3/2}$
Ni II	1000	59	51812	$3d^8(^3F)7f\ ^4I^o_{9/2}$
Ni III	1000	42	66511	$3d^7(^2D)4d\ ^3S_1$
Ni IV	254	28	6317	$3D^6(^1G_1)4p\ ^2G^o_{7/2}$
Ni V	183	46	3065	$3d^5(^2D3)4p\ ^3F^o_3$
Ni VI	314	37	9569	$3d^4(^5D)4d\ ^4F_{9/2}$
Ni VII	308	37	9225	$3d^3(^2D)4d\ ^3P_2$
Total	**18 710**	**2534**	**1 717 141**	